Applied Energy 268 (2020) 115014

Contents lists available at ScienceDirect

Applied Energy

journal homepage: www.elsevier.com/locate/apenergy

Characterisation of aeroelastic harvester efficiency by measuring transient growth of oscillations

S. Tucker Harvey[a,*], I.A. Khovanov[a], Y. Murai[b], P. Denissenko[a]

[a] School of Engineering, University of Warwick, Coventry CV4 7AL, United Kingdom
[b] Laboratory for Flow Control, Faculty of Engineering, Hokkaido University, N13-W8, Kita-ku, Sapporo 0608628, Japan

HIGHLIGHTS

- A method for estimating harvesting performance from the free transient is developed.
- Curved blade is shown to be an order of magnitude more efficient than square prism.
- The optimal curvature range of the galloping curved blade harvester is established.
- Flow attachment is shown to improve performance of galloping energy harvesters.
- The cyclic formation and shedding of a leading edge vortex is documented.

ARTICLE INFO

Keywords:
Galloping
Energy Harvesting
Curved blade
Aerodynamics

ABSTRACT

With growing demand for small autonomous electrical devices, such as those in wireless sensor networks, energy harvesting has attracted interest with the promise of low maintenance and sustainable power sources. Galloping energy harvesters utilise the fluid-structure interaction to transform kinetic energy in fluid flow into electrical energy. The performance of galloping energy harvesters depends on the geometry of the tip, with the structure of the flow around the tip defining the nature of fluid-structure interaction and hence the potential efficiency of the device.

In this work the curved blade tip geometry is investigated. To experimentally characterise the performance of the harvester, a method utilising the free oscillation transient is developed. The method avoids implementation of a transduction mechanism and hence optimisation of the associated parameters. The developed method is generic and can be applied to other energy generators.

The power coefficient of curved blades of different curvatures is measured and the optimal range identified. The maximum coefficient of performance of the curved blade harvester occurs at tip speed ratios from 0.32 to 0.74 and reaches 0.08, which is 3 to 4 times lower than Savonius turbines, the best performing devices at similar Reynolds numbers. The square prism geometry is used as a comparator and found to have a coefficient of performance 10 times less than the curved blade. Flow visualisations confirm the curved blade to act as an airfoil in the highest performing cases, hence future tip shapes should be developed to promote flow attachment.

1. Introduction

The objective of energy harvesting is to convert ambient energy to a useable form, typically electrical energy for use in small electrical devices. Interest in energy harvesting technologies has grown rapidly in recent years as demand for small autonomous electrical devices, such as those in wireless sensor networks, has increased. Energy harvesting systems can enable the avoidance of chemical batteries and their drawbacks [1], with applications varying from roadway engineering [2] to wearable devices [3].

As applications of energy harvesting vary so significantly, no single energy source can be considered as optimal for all cases, but rather the best energy source is likely to be specific to a particular application. A range of energy sources have hence been considered including solar energy [4], thermal energy [5] and kinetic energy in fluid flow [6]. Further to this combining different sources into a single device has also been shown to be an effective approach, for example the combination of fluid flow and mechanical vibration [7] or fluid flow and solar energy [8].

* Corresponding author.
E-mail address: samtuckerharvey@live.com (S. Tucker Harvey).

https://doi.org/10.1016/j.apenergy.2020.115014
Received 4 December 2019; Received in revised form 4 April 2020; Accepted 7 April 2020
Available online 24 April 2020

Aeroelastic energy harvesting utilises fluid-structure interaction to transform kinetic energy in fluid flow into a useable form and can broadly be distinguished into three phenomenon, vortex induced vibrations [9], the flutter of aerofoils [10] and the galloping instability of prismatic sections [11]. Vortex induced vibrations occur due to the unsteady periodic shedding of vortices from a structure, which results in a periodic forcing that may lead to resonant oscillations. Aerofoil flutter occurs as the coupled two degree of freedom dynamics of the aerofoil results in the formation of self-sustained oscillations. The galloping instability only requires a single degree of freedom and can also lead to the formation of self-sustained oscillations under incident flow conditions [12]. These self-sustained oscillations can be exploited for the harvesting of flow energy by the implementation of an appropriate transduction mechanism, typically based on either the piezoelectric effect [13] or electromagnetic induction [14].

The tip geometry of the galloping energy harvester fundamentally determines the nature of the fluid-structure interaction and hence the potential energy harvesting performance. A variety of geometries have been considered, particularly the rectangular [15], isosceles triangular [16] and D-shaped [17] prismatic sections. Experimental comparison of these geometries has demonstrated the square prism to provide the greatest power output [18]. Modifications to the circular cylinder by the attachment of cylindrical rods has also been demonstrated to result in galloping oscillations [19], rather than oscillations purely induced by the periodic shedding of vortices. Other geometries, such as the fork-shaped design developed by Liu, Zhang, Peng and Meng [20] and the curved plate geometry of Zhou, Zou, Wei and Liu [21], have more recently been demonstrated to be capable of high harvesting efficiencies.

Dissimilarly to the detached bluff body flows which are observed for the rectangular, isosceles triangular and D-shaped sections, in the case of the curved blade tip geometry suggested in Tucker Harvey, Khovanov and Denissenko [22], the flow becomes attached to the rear face of the geometry and results in improved harvesting efficiencies. The curvature of the blade is a key geometric parameter for defining its aerodynamics and hence whether the flow becomes attached. As previous investigations of the galloping curved blade considered only a single curvature, the role of curvature forms a significant knowledge gap in the development of these devices, which is addressed in the current study.

In this work, the influence of the curvature of the galloping curved blade on energy harvesting performance is evaluated experimentally. Dissimilarly to other experimental assessments of the performance of galloping energy harvesters, where a transduction mechanism was implemented and optimised to allow the measurement of harvested power [15], an approach is developed to the predict the performance from the free oscillation transient without a transduction mechanism. This avoids the influence of the particular implementation of a transduction mechanism as well as the requirement of optimising its parameters. This suggested alternative method could be applied to many other similar devices, while the results identify the optimal curvatures for the curved blade geometry.

The nature of the flow field around the blade is examined through flow visualisation. This methodology allows the different flow structures to be readily identified and related to the variation of performance and avoids the use of computationally expensive simulations. The visualisations demonstrate clear distinctions in the flow field between the lower and higher performing curvatures. The operational regime of the latter is related to that of wind turbines. To provide a reference to geometries which have been previously considered in the literature, a square prism geometry is also evaluated and compared to results obtained with the curved blade.

In this paper, the experimental methodology applied to capture the transient and steady state dynamics of the galloping oscillators is first described in Section 2. Following this the method for the prediction of the energy harvesting performance from the free oscillation transient is derived from the underlying mathematical model in Section 3, alongside the results of a numerical verification. The experimental results are presented in Section 4, with both the steady state dynamics and predicted energy harvesting performance. Finally, flow visualisations for the different geometries are illustrated in Section 5.

2. Experimental methodology

The galloping oscillator was constructed by fixing a 3D printed curved blade to the end of two cantilever beams. The curved blades of different curvatures were manufactured with an UP BOX 3D printer using acrylonitrile butadiene styrene (ABS) as the extruded material. The oscillator could then be mounted into a wind tunnel where flow conditions could be closely controlled, and aligned such that oscillations occur in a direction perpendicular to the freestream flow direction. Fig. 1 demonstrates the constructed galloping oscillator and its orientation with relation to the freestream flow velocity, which is denoted by U_∞, while the detailed experimental setup within the wind tunnel test section is illustrated in Fig. 2.

The geometry of the curved blade was defined by a circular arc of base radius R and arc angle 2γ. The curvature could hence be defined by

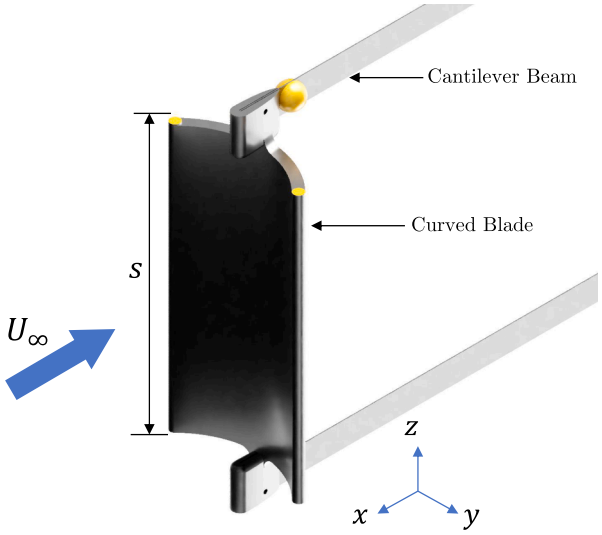

Fig. 1. A galloping oscillator. The curved blade oscillates in the x, y plane. U_∞ denotes the freestream flow velocity, while s is the span of the curved blade. The fluorescent markers are illustrated with a yellow colour.

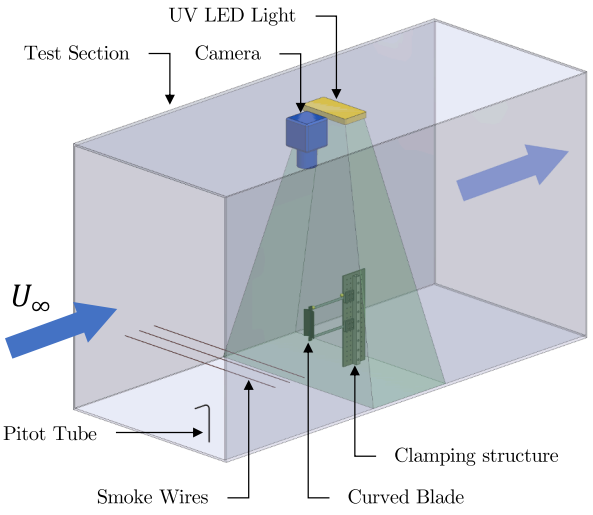

Fig. 2. Experimental setup inside wind tunnel test section. The blue arrows demonstrate the flow direction. U_∞ denotes the freestream flow velocity.

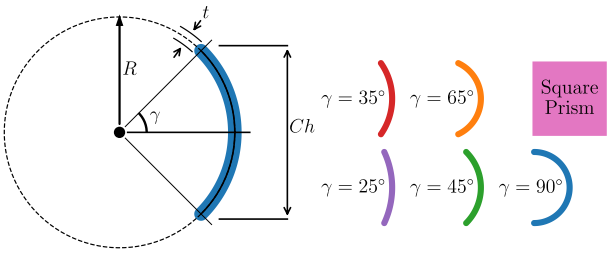

Fig. 3. Definition of blade section geometry and illustration of selected range of curvatures. Square prism cross-section is shown for comparison.

Table 1
Parameters of experimental galloping oscillator.

Parameter	Sym	Value (unit)
Blade Mass	m_{tip}	40×10^{-3} (Kg)
Oscillation Frequency	ω	19.7 ($rads^{-1}$)
Blade Half Arc Angle	γ	25°, 35°, 45°, 65°, 90°
Blade Base Circle Radius	R	81, 60, 49, 38, 34 (mm)
Blade Chord Length	Ch	75 (mm)
Blade Thickness	t	5 (mm)
Blade Span	s	75 (mm)
Beam Length	l_b	212 (mm)
Beam Width	w_b	12.5 (mm)
Beam Thickness	t_b	0.5 (mm)

the half arc angle γ as demonstrated in Fig. 3. A range of angles from 90° to 25° were selected for the analysis. For a comparison to be made between blades of different curvature, the chord length, Ch, span, s, and thickness, t, of the blade were maintained constant between the geometries. The blade mass m_{tip} was also kept constant to ensure that the oscillation frequency was the same throughout the experiments. This was achieved by varying the infill percentage in the 3D printing process. The parameters of the experimental system are presented in Table 1.

A simplified two dimensional illustration of the galloping oscillator is demonstrated in Fig. 4, which also shows the aerodynamic forces and velocity vectors. The galloping instability occurs due to the change in the aerodynamic forces acting on the blade with the effective angle of attack α, which is defined as,

$$\alpha = \tan^{-1}\left(\frac{\dot{y}}{U_\infty}\right) - \psi \tag{1}$$

where $\dot{y}$ denotes the velocity of the blade in the y direction and ψ is the maximum slope angle of the beam. This relationship is illustrated in Fig. 4.

To provide a comparison to geometries which have been previously studied in the literature, a square prism geometry was constructed with width and length equal to the curved blade chord length. The mass and

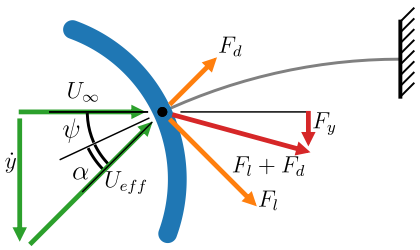

Fig. 4. Velocity vectors and forces acting on the curved blade. The blade is rotated by the maximum slope angle of the beam, ψ. U_{eff} denotes the effective flow velocity. The lift force and drag force are represented by F_l and F_d respectively, while the aerodynamic force projected in the y direction is denoted by F_y.

span of the square geometry were also fixed to that of the curved blades.

The dynamics of the oscillator were captured with the use of a single camera motion tracking system with four fluorescent markers under ultraviolet illumination. The positions of the camera and UV light within the wind tunnel test section are demonstrated in Fig. 2. The camera, which was positioned above the galloping oscillator, had a frame rate of 50 fps and a resolution of 1920×1080 pixels. The first marker was positioned at the base of the cantilever beam, acting as a datum. The second marker was placed at the top of the cantilever beam, providing the position of the blade, while the two remaining markers provided the locations of the blade tips, which allowed the maximum slope angle of the cantilever beam ψ to be determined. The maximum uncertainty of the motion tracking was estimated at 1.8 mm, which is equivalent to 0.026 when nondimensionalised with chord length Ch.

The flow velocity within the wind tunnel was varied from 0.9 ms^{-1} to 2.0 ms^{-1} corresponding to Reynolds numbers of 4.0×10^3 and 9.0×10^3 respectively. The Reynolds number is defined as,

$$Re = \frac{\rho U_\infty Ch}{\mu} \tag{2}$$

where ρ and μ are the density and dynamic viscosity of air respectively. Flow velocity measurements were made within the test section of the wind tunnel with a pitot tube connected to a Furness Controls FCO560 digital manometer. Measurements were taken at a sampling frequency of 100 Hz with an estimated maximum uncertainty of 0.012 ms^{-1}. The dynamics of the galloping oscillator were acquired from rest under constant flow velocity conditions, providing both the transient and steady state dynamics.

Smoke wire flow visualisation was performed to allow the observation of the flow patterns around the different blade geometries. A Phantom high speed camera captured images at a frame rate of 600 fps and with a resolution of 1152×896 pixels, while smoke was generated by a twisted pair of 0.255 mm diameter steel wires, which was coated with mineral oil and mounted horizontally across the wind tunnel test section. An electrical current was then put through the wires to vaporise the oil, hence seeding the flow. The location of the smoke wires relative to the galloping oscillator is illustrated in Fig. 2.

3. Predicting energy harvesting performance from the free oscillation transient

To demonstrate how the performance of a galloping energy harvester can be predicted from the free oscillation transient, the underlying mathematical model must first be considered. The dynamics of a galloping energy harvester with a piezoelectric harvesting circuit have been shown to be well described by the system of Ordinary Differential Equations (ODEs) [23],

$$\ddot{y} - \frac{\rho A_f}{2m_{tip}} C_y(\alpha)(\dot{y}^2 + U_\infty^2) + \frac{C_{damp}}{m_{tip}} + \omega^2 y - \frac{\theta}{m_{tip}} V = 0 \tag{3}$$

$$\dot{V} = -\frac{1}{C_p}\left(\frac{V}{R_l} + \theta\dot{y}\right) \tag{4}$$

where $C_y(\alpha)$ is the force coefficient of the projection of the aerodynamic force in the y direction, A_f is the projected frontal area of the tip geometry, C_{damp} is the mechanical damping coefficient and ω denotes the oscillation frequency. In the second equation, which describes the harvesting circuit, θ represents the electromechanical coupling factor, V is the voltage generated across the piezoelectric, R_l is the resistance of the load resistor and C_p is the capacitance of the piezoelectric. An equation in terms of instantaneous power can be obtained by multiplying Eq. (3) by the linear velocity $\dot{y}$ and the tip mass m_{tip} yielding,

$$m_{tip}\dot{y}\ddot{y} - \frac{\rho A_f}{2} C_y(\alpha)(\dot{y}^2 + U_\infty^2)\dot{y} + C_{damp}\dot{y}^2 + m_{tip}\omega^2 y\dot{y} - \theta V\dot{y} = 0 \tag{5}$$

Assuming the trajectory is periodic with a frequency of ω, Eq. (5) can be cycle averaged by integrating temporally between 0 and $\frac{2\pi}{\omega}$ yielding,

$$\frac{\omega}{2\pi}\int_0^{\frac{2\pi}{\omega}} m_{tip}\dot{y}\ddot{y}\,dt - \frac{\omega}{2\pi}\int_0^{\frac{2\pi}{\omega}} \frac{\rho A_f}{2} C_y(\alpha)(\dot{y}^2 + U_\infty^2)\dot{y}\,dt + \frac{\omega}{2\pi}\int_0^{\frac{2\pi}{\omega}} C_{damp}\dot{y}^2\,dt + \frac{\omega}{2\pi}\int_0^{\frac{2\pi}{\omega}} m_{tip}\omega^2 y\dot{y}\,dt - \frac{\omega}{2\pi}\int_0^{\frac{2\pi}{\omega}} \theta V\dot{y}\,dt = 0 \tag{6}$$

The total energy in the galloping oscillator E_{tot} can be defined as the sum of the kinetic and potential energies,

$$E_{tot} = \frac{1}{2}m_{tip}\dot{y}^2 + \frac{1}{2}m_{tip}\omega^2 y^2 \tag{7}$$

Taking the time derivative and cycle averaging yields,

$$\frac{d\overline{E}_{tot}}{dt} = \frac{2\pi}{\omega}\int_0^{\frac{2\pi}{\omega}} m_{tip}\dot{y}\ddot{y}\,dt + \frac{2\pi}{\omega}\int_0^{\frac{2\pi}{\omega}} m_{tip}\omega^2 y\dot{y}\,dt \tag{8}$$

Substituting into Eq. (6) yields,

$$\frac{d\overline{E}_{tot}}{dt} - \overbrace{\frac{\omega}{2\pi}\int_0^{\frac{2\pi}{\omega}} \frac{\rho A_f}{2} C_y(\alpha)(\dot{y}^2 + U_\infty^2)\dot{y}\,dt}^{\overline{P}_{fs}} + \overbrace{\frac{\omega}{2\pi}\int_0^{\frac{2\pi}{\omega}} C_{damp}\dot{y}^2\,dt}^{\overline{P}_{damp}} - \overbrace{\frac{\omega}{2\pi}\int_0^{\frac{2\pi}{\omega}} \theta V\dot{y}\,dt}^{\overline{P}_{elec}} = 0 \tag{9}$$

Here $\overline{P}_{fs}$, $\overline{P}_{damp}$ and $\overline{P}_{elec}$ denote the cycle averaged power flows due to fluid-structure interaction, mechanical damping and electromechanical interaction respectively. Similar consideration of Eq. (4), which describes the harvesting circuit, provides a second cycle averaged power equation which can be written as,

$$\overbrace{\frac{\omega}{2\pi}\int_0^{\frac{2\pi}{\omega}} C_p V\dot{V}\,dt}^{\frac{d\overline{E}_{cap}}{dt}} = \overbrace{\frac{\omega}{2\pi}\int_0^{\frac{2\pi}{\omega}} \frac{-V^2}{R_l}\,dt}^{\overline{P}_{harv}} - \overbrace{\frac{\omega}{2\pi}\int_0^{\frac{2\pi}{\omega}} \theta\dot{y}V\,dt}^{\overline{P}_{elec}} \tag{10}$$

where $\overline{P}_{harv}$ denotes the cycled averaged harvested power and $\frac{d\overline{E}_{cap}}{dt}$ is the cycle averaged time derivative of the power contained within the capacitor in the circuit. Combining the two cycle averaged equations in terms of power flows yields,

$$\frac{d\overline{E}_{tot}}{dt} - \overline{P}_{fs} + \overline{P}_{damp} = -\frac{d\overline{E}_{cap}}{dt} - \overline{P}_{harv} \tag{11}$$

Provided there is significant time scale separation between the conservative and non-conservative terms the system can be considered as weakly nonlinear and hence the trajectory can be approximated as sinusoidal,

$$y = A_y\sin(\omega t), \quad V = A_V\sin(\omega t + \phi) \tag{12}$$

where A_y denotes the amplitude of the y displacement, A_V is the amplitude of the voltage in the harvesting circuit and ϕ is the phase difference between the displacement and the voltage. Under this assumption, it can be shown that all terms in Eq. (11) become functions of the displacement amplitude A_y only and hence the power flow is defined by the oscillation amplitude and the parameters. When the system is operating on a limit cycle, hence with constant amplitude, and energy is harvested with $\theta > 0$, there cannot be cycle averaged accumulation of energy within either the electrical circuit or the galloping oscillator resulting in,

$$\frac{d\overline{E}_{tot}}{dt} = 0, \quad \frac{d\overline{E}_{cap}}{dt} = 0 \tag{13}$$

This results in the simplification of Eq. (11) to,

$$\overline{P}_{fs} - \overline{P}_{damp} = \overline{P}_{harv} \tag{14}$$

Alternatively, considering a case without energy harvesting, hence $\theta = 0$, and in which oscillations are growing in amplitude,

$$\frac{d\overline{E}_{tot}}{dt} = \overline{P}_{fs} - \overline{P}_{damp} \tag{15}$$

Comparing Eqs. (14) and (15) and considering that the terms are functions of the oscillation amplitude A_y only with the assumption of a sinusoidal trajectory,

$$\left.\frac{d\overline{E}_{tot}}{dt}\right|_{\theta=0} = \left.\overline{P}_{harv}\right|_{\theta>0} \tag{16}$$

Under the condition that the steady state amplitude when $\theta > 0$ is equal to the instantaneous amplitude when $\theta = 0$,

$$A_y(\theta = 0) = A_y(\theta > 0) \tag{17}$$

The cycle averaged accumulation of total energy within a galloping oscillator $\frac{d\overline{E}_{tot}}{dt}$ without a harvesting mechanism therefore provides an estimate of the power which could be harvested at the same instantaneous amplitude, A_y, if a mechanism where to be implemented and harvested energy under steady state conditions, whilst maintaining constant amplitude.

The method for estimating power was verified with numerical simulations of the underlying ODEs, Eqs. (3) and (4), while utilising the polynomial approximation of C_y for the square cylinder tip geometry developed by Parkinson [12]. Typically parameters for the galloping oscillator and harvesting circuit where taken from Yang, Zhao and Tang [18]. A transient with $\theta = 0$ was first simulated and then used to predict the harvesting power $\overline{P}_{harv}$ as a function of amplitude A_y. These results were then compared to steady state simulations of the system with $\theta > 0$. Both small perturbation and large displacement initial conditions were utilised for these simulations to ensure the discovery of all limit cycles. Fig. 5 demonstrates the verification results at three different reduced velocities. Reduced velocity is defined as,

$$U^* = \frac{2\pi U_\infty}{\omega Ch} \tag{18}$$

where Ch is the chord length of the blade. Similarly to wind turbines, a tip speed ratio can be defined as,

$$u_{ts} = \frac{\dot{y}}{U_\infty}, \quad U_{ts} = \frac{\dot{Y}}{U_\infty} \tag{19}$$

u_{ts} represents the ratio based on instantaneous velocity $\dot{y}$, whereas U_{ts} is based on velocity amplitude $\dot{Y}$ and hence provides a maximum speed

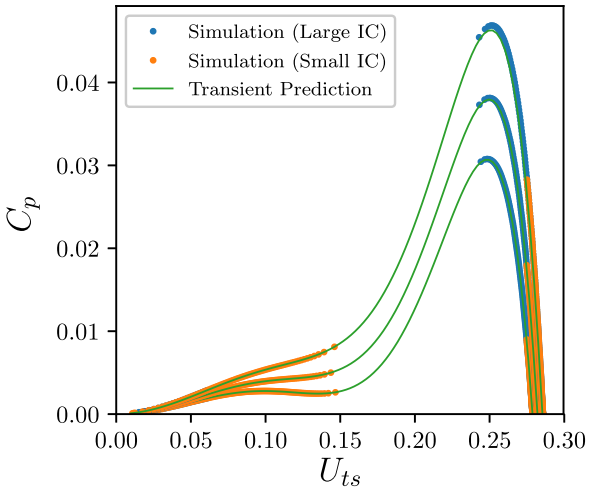

Fig. 5. Comparison of simulated energy harvesting performance and free transient prediction. Results are shown for reduced velocities of 10.3, 12.8 and 17.6 with C_p increasing between each of the cases. Results obtained with both small perturbation (Small IC) and large displacement (Large IC) initial conditions are shown.

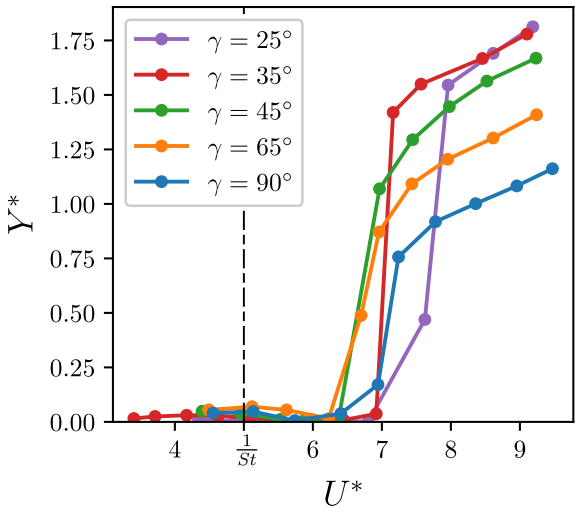

Fig. 6. Steady state oscillation amplitude vs reduced velocity. The displacement amplitude is nondimensionalised with chord length as $Y^* = \frac{Y}{Ch}$. A dashed vertical line marks the reduced velocity of $\frac{1}{St}$, where $St = 0.2$. A reduced velocity of 8.0 corresponds to a freestream flow velocity of 1.7 ms^{-1}.

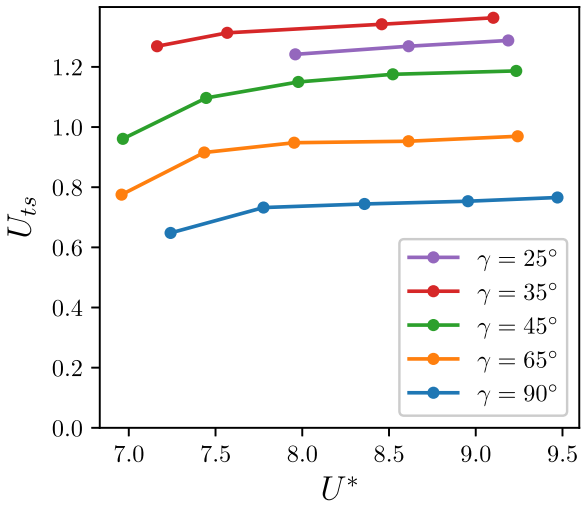

Fig. 7. Maximum tip speed ratio vs reduced velocity. With the amplitude of oscillations growing with reduced velocity, the amplitude of tip speed ratio tends to a constant.

ratio. Harvested power can be nondimensionalised with the coefficient of performance C_p,

$$C_p = 2\frac{P_{harv}}{\rho A_{swept} U_\infty^3} \tag{20}$$

where A_{swept} is the frontal area which the blade travels through. The prediction based on the free oscillation transient can be seen to accurately predict the harvested power when the model was simulated with $\theta > 0$.

4. Experimental dynamics and estimated harvesting performance

Fig. 6 illustrates the steady state limit cycle amplitudes, as measured by the y displacement, with reduced velocity.

For all the investigated curvatures, large amplitude galloping oscillations occur only after a region of vortex induced vibrations which exists around the reduced velocity of $\frac{1}{St}$ where St is the Strouhal number which can be defined as,

$$St = \frac{f_s Ch}{U_\infty} \tag{21}$$

where f_s is the shedding frequency. In this region the frequency of vortex shedding f_s becomes close to the oscillation frequency $2\pi\omega$, hence resulting in small resonant oscillations. After this region, the amplitude of the limit cycles can be seen to decrease with the curvature half arc angle γ, while the minimum flow velocity required to lead to the formation of galloping oscillations was greatest for the least curved geometries. As the range of evaluated reduced velocities is not significantly larger than $\frac{1}{St}$, unsteady aerodynamic effects are likely to have a significant influence across the full range, while it is also possibly that vortex induced vibrations delayed the onset of galloping oscillations due to quenching.

Fig. 7 demonstrates the maximum tip speed ratio with reduced velocity. For all of the considered geometries, it is noticeable that the maximum speed ratio U_{ts} appears to tend to a constant value with reduced velocity. It can be shown that in the case of a galloping oscillator where the angle of attack is a function of u_{ts} only with $\alpha = \tan^{-1}(u_{ts})$ and the cantilever beam orientated perpendicular to U_∞, the amplitude U_{ts} on the limit cycle will become constant with reduced velocity as aerodynamics dominates the influence of mechanical damping. This has also been demonstrated experimentally in previous investigations of the galloping curved blade [22]. As Fig. 7 shows a similar behaviour, it can be suggested that the most significant period of power flow, which defines the limit cycle amplitude, occurs when ψ is close to zero. This would hence provide a similar dependence of U_{ts} on U^* as when α is a function of u_{ts} only, where the deflection of the beam does not result in a rotation of the tip geometry which contributes to the angle of attack.

Fig. 8 illustrates how the angle of attack varies with the tip speed ratio on the steady state limit cycle at a number of different reduced velocities. The cycles tend to a constant value at the u_{ts} maximas, which is consistent with the tending of U_{ts} to a constant value in Fig. 7. The maximum values of α occur below the maximum value of u_{ts} and hence correspond to the combined influence of both beam deflection and the velocity of the blade.

The calculation of $\frac{d\overline{E}_{tot}}{dt}$ for the estimation of the energy harvesting performance is illustrated for an individual transient in Fig. 9. The top plot demonstrates the time series of the centre of mass displacement nondimensionalised by the chord length, $y^* = y/Ch$. Time is nondimensionalised by the oscillation time period, $t^* = 2\pi\omega t$. The second plot presents the cycle averaged total energy $\overline{E}_{tot}$. This can be seen to grow from zero, where there are no oscillations, to a constant value, where the oscillations are on the limit cycle. The rate at which $\overline{E}_{tot}$

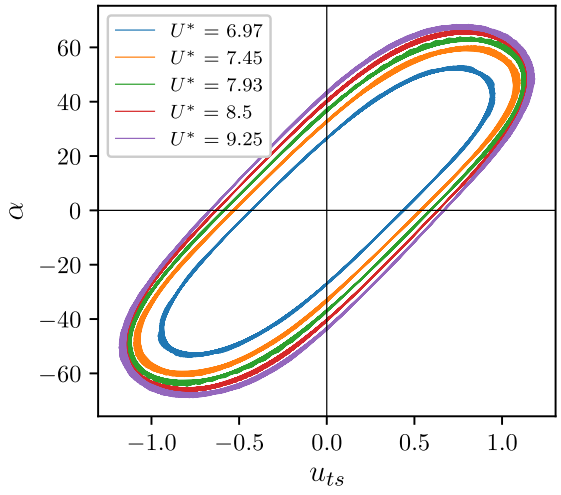

Fig. 8. Angle of attack vs tip speed ratio on the limit cycle for the 45° half arc angle geometry. The deviation of the trajectory from a straight line occurs due to dependance of angle of attack on the maximum beam slope angle and hence tip displacement, as shown in Fig. 4.

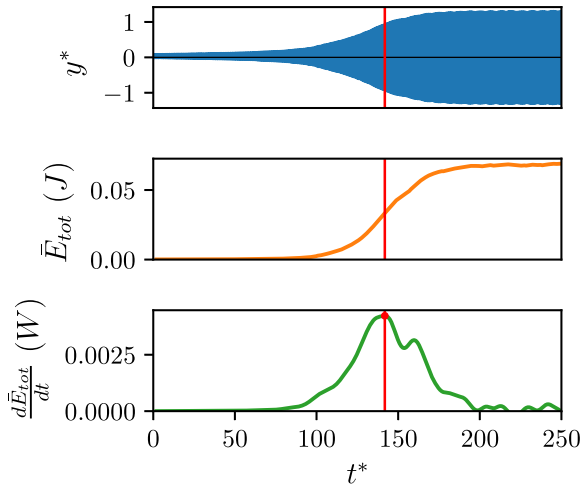

Fig. 9. Illustration of calculation of $\frac{d\bar{E}_{tot}}{dt}$. Time is nondimensionalsed with time period as $t^* = 2\pi\omega t$, while y displacement is nondimensionalised with chord length as $y^* = y/Ch$.

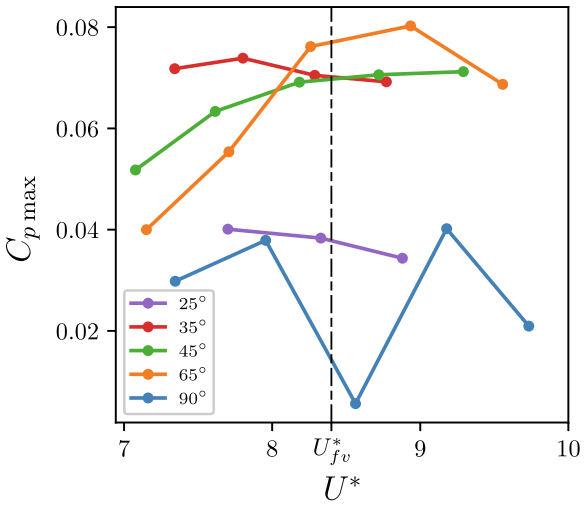

Fig. 11. Maximum C_p with reduced velocity. U^*_{fv} illustrates the reduced velocity at which flow visualisations were performed. A reduced velocity of 8.0 corresponds to a freestream flow velocity of 1.7 ms^{-1}.

grows with time can be seen to be small at the start of the transient and small close to the limit cycle but with a maximum between. The third plot illustrates the cycle averaged time derivative $\frac{d\bar{E}_{tot}}{dt}$, which provides the estimate of energy harvesting performance. The amplitude at which cycle averaged energy growth is fastest and hence the energy harvesting performance would be greatest is marked by the red line.

The dependence of the estimated coefficient of performance C_p on the tip speed ratio for the different geometries considered is presented in Fig. 10. Results obtained at three different reduced velocities are shown, as illustrated by dotted, dashed and solid lines. The 35°, 45° and 65° geometries can be seen to significantly outperform the other two. The curves for the three different reduced velocities also appear to be close to collapsing, especially for the 45° and 65° curvatures. This collapse would be expected in the case where the cantilever beam is perpendicular to U_∞ and hence suggests that the most significant point for power flow within the cycle is when ψ is close to zero.

The optimal operating amplitude for energy harvesting is defined by the location of the C_p maximum. The tip speed ratio U_{ts} at the C_p maximum was greatest for the 35° geometry with an average of 0.76, while the lowest values occurred with the 90° geometry with an average of 0.45.

The maxima of C_p with reduced velocity is illustrated in Fig. 11 for the different curvature geometries. The 35°, 45° and 65° geometries can be seen to substantially outperform the other two geometries for all considered reduced velocities. The leading of the two varied with reduced velocity, with the 35° geometry leading at lower velocities, while the 65° geometry performed best at the higher end of the reduced velocity range.

A comparison of performance of the curved blade and the square prism geometry is demonstrated in Fig. 12. All of the evaluated curved blade geometries can be seen to substantially outperform the square prism, which operates at a much lower tip speed ratio. Comparing the performance of the curved blade to that of rotating wind energy devices demonstrates it to be positioned at a C_p value of close to half that of an American Multiblade turbine and only three to four times below Savonius turbines [24].

5. Flow visualisation

Flow visualisations for the five considered curvatures are illustrated in Fig. 13 at a reduced velocity of 8.4. The blade is viewed from above, with the freestream flow direction in the upward direction. The blade is

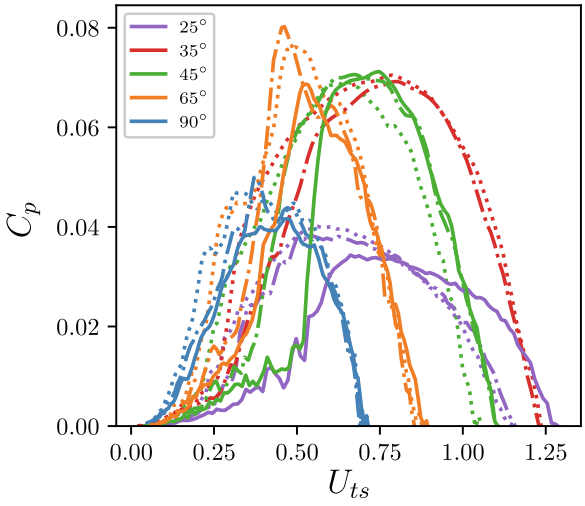

Fig. 10. Estimated coefficient of performance C_p with tip speed ratio. Dotted lines represent results acquired at a reduced velocity of 8.0, dashed lines at a reduced velocity of 8.7 and solid lines at reduced velocity of 9.3.

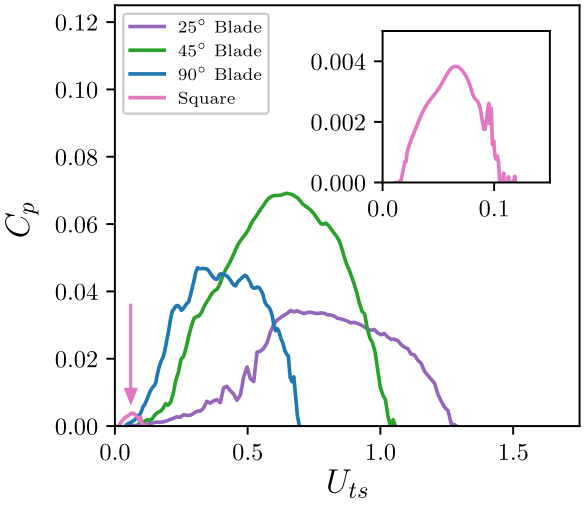

Fig. 12. Comparison of estimated coefficient of performance C_p with tip speed ratio between the curved blade and square prism geometries. The arrow illustrates the position of the square prism curve.

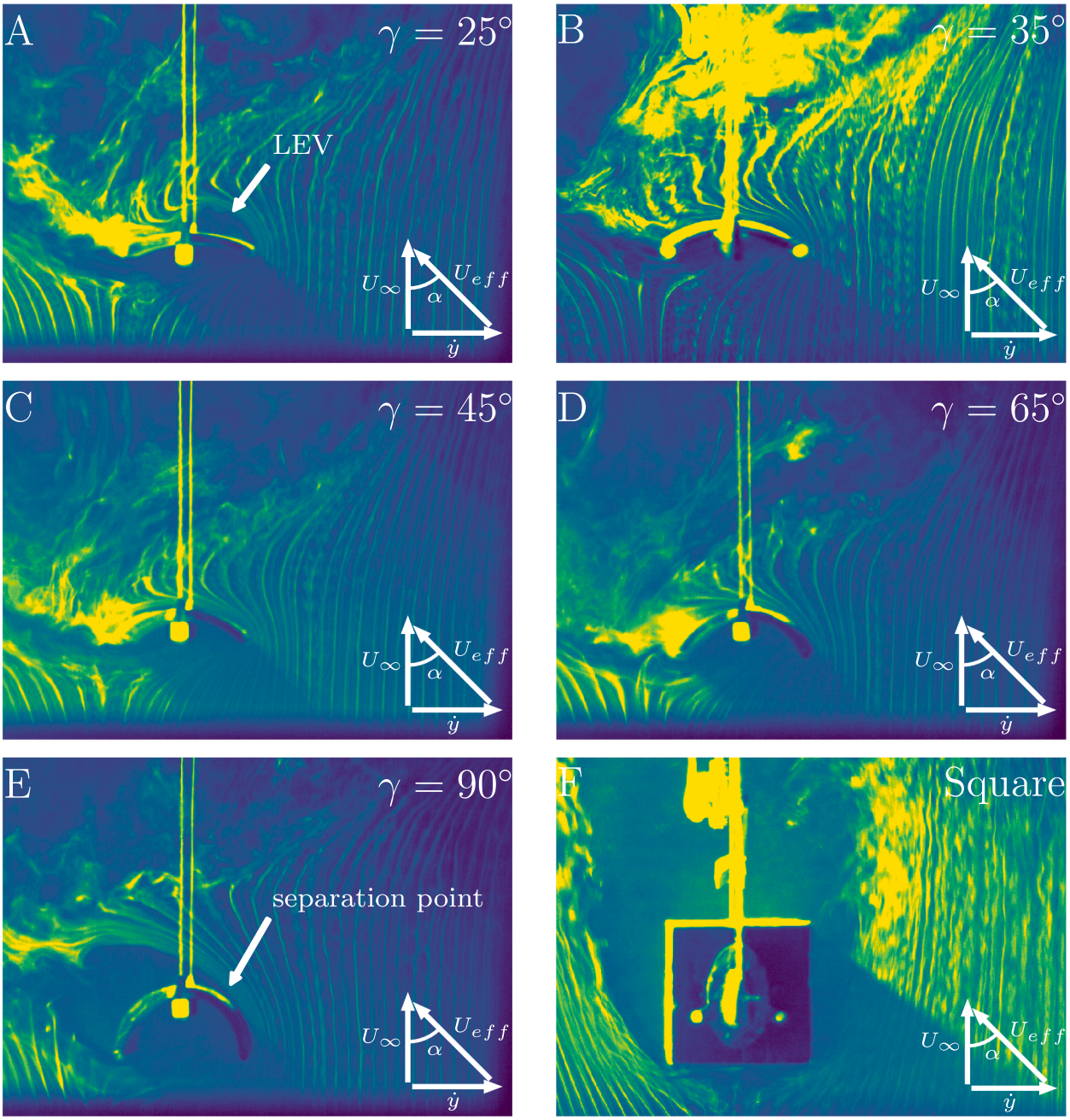

Fig. 13. Flow visualisations with different curvatures and with the square prism geometry. Reduced velocity $U^* = 8.4$. The colourmap represents the pixel intensity values obtained from the monochrome Phantom high speed camera. The flow can be seen to be attached to the rear surface of the blade in B, C and D but not in A and E. The formation of a Leading Edge Vortex (LEV) is evident in A, corresponding to the least curved geometry.

close to its zero displacement position and is traveling from left to right. The colourmap represents the pixel intensities obtained from the monochrome Phantom high speed camera and is used to improve the clarity of the visualisations. The twisted wires generated a series of filaments of smoke, rather than a continuous sheet. These filaments of smoke represent streaklines, defined as the loci of points of all the fluid particles which have passed through a particular point in the past, and are clearly illuminated in Fig. 13. When unperturbed by the presence of the blade, the streaklines appear straight, reflecting only the freestream uniform flow. This is evident in the right hand side of the visualisations. Closer to the blade the streaklines are deflected significantly. The deflection of the streaklines in the left direction on the rear surface of the blades is illustrative of the generation of a force in the *y* direction acting on the blade. Dark regions in the visualisations illustrate areas where the smoke is well mixed due to higher vorticity in these areas.

In subplot A, which relates to the least curved geometry with an arc angle of 25°, leading edge separation is evident as well as the formation of a large leading edge vortex (LEV). In subplots B, C and D, which relate to the higher performing 35°, 45° and 65° half arc angle geometries, leading edge flow separation is not evident and the flow appears to be attached for the majority of the chord length. Subplot E demonstrates the geometry with the highest curvature, relating to a half arc angle of 90°. In this case the separation point is close to the leading edge resulting in the formation of a large wake.

In the square prism case, illustrated in subplot F of Fig. 13, the flow can be seen to separate on both of the front edges of the square without reattachment on the sides parallel to the freestream flow direction. The stagnation point can also be seen to be close to the centre of the front face. The flow in the case of the square prism is hence highly separated, differing significantly from the attached flows observed with the

35°, 45° and 65° half arc angle curved blade geometries.

It can hence be concluded that the attachment of the flow to the rear surface of the blade allows the 35°, 45° and 65° arc angle geometries to outperform the others considered. The formation and shedding of a leading edge vortex during each half oscillation was evident for the 25°, 35°, 45° and 65° cases and could provide a lift enhancement in these cases by similar mechanisms to as has been shown to occur in flapping flight [25,26]. However, the unsteady forces relating to the leading edge vortex and how they relate to energy harvesting performance requires further investigation.

6. Conclusions

In this work, the influence of curvature on the energy harvesting performance of the galloping curved blade has been investigated experimentally by measuring the growth rate of total energy in the free oscillation transient. The developed method avoids the implementation of a transduction mechanism and hence the optimisation of the associated parameters, providing a convenient and fast means of evaluating the energy harvesting performance of galloping geometries. The method could hence be applied to similar geometries and aid in their experimental development.

The curved blades with curvatures in the medium range, with half arc angles of 35°, 45° and 65° were found to considerably outperform curved blades with 25° and 90° half angles. As demonstrated by flow visualisations, the flow becomes attached in these three cases but not in the others. The higher performance in these cases can hence be attributed to the attachment of the flow to the rear surface of the blade when the velocity is close to its maxima. A maximum coefficient of performance of 0.08 was obtained with the 65° half arc angle geometry. The optimal operating amplitude of a wind energy harvester is defined by the amplitude of the coefficient of performance maximum. For the curved blades investigated, the tip speed ratio at the coefficient of performance maximum ranged from 0.32 to 0.74.

Comparison of the curved blade to the square prism geometry, which has been shown to relate to a highly separated flow, has demonstrated the curved blade to provide an order of magnitude higher performance within the considered range of reduced velocities.

Flow visualisations have also demonstrated the presence of a leading edge vortex, which is formed and shed during each half oscillation and occurs with four of the five investigated geometries. Although the leading edge vortex may provide a lift enhancement, further investigation is required to determine whether it is beneficial to energy harvesting performance.

The results hence demonstrate that when designing galloping energy harvesters based on the curved blade geometry, half arc angles of around 65° will provide the greatest harvesting efficiencies. The measured coefficient of performance of 0.08 places the curved blade harvester only three to fours times below Savonius turbines, making it a candidate for real world applications.

This work was supported by the Engineering and Physical Sciences Research Council under Grant No. EP/N509796/1 and Daiwa Anglo-Japanese Foundation under Award No. 6842/13830. Data related to this research are openly available at https://wrap.warwick.ac.uk/136068.

CRediT authorship contribution statement

S. Tucker Harvey: Conceptualization, Methodology, Software, Formal analysis, Investigation, Writing - original draft, Writing - review & editing, Visualization. **I.A. Khovanov:** Supervision, Conceptualization, Writing - review & editing. **Y. Murai:** Conceptualization, Writing - review & editing. **P. Denissenko:** Supervision, Conceptualization, Writing - review & editing.

Declaration of Competing Interest

The authors declare that they have no known competing financial interests or personal relationships that could have appeared to influence the work reported in this paper.

References

[1] Halim M, Rantz R, Zhang Q, Gu L, Yang K, Roundy S. An electromagnetic rotational energy harvester using sprung eccentric rotor, driven by pseudo-walking motion. Appl Energy 2018;217:66–74. https://doi.org/10.1016/j.apenergy.2018.02.093.
[2] Gholikhani M, Roshani H, Dessouky S, Papagiannakis A. A critical review of roadway energy harvesting technologies. Appl Energy 2020;261:114388. https://doi.org/10.1016/j.apenergy.2019.114388.
[3] Nozariasbmarz A, Collins H, Dsouza K, Polash MH, Hosseini M, Hyland M, Liu J, Malhotra A, Ortiz FM, Mohaddes F, Ramesh VP, Sargolzaeiaval Y, Snouwaert N, zturk MC, Vashaee D, et al. Review of wearable thermoelectric energy harvesting: From body temperature to electronic systems. Appl Energy 2020;258:114069. https://doi.org/10.1016/j.apenergy.2019.114069.
[4] Jia H, Cheng X, Zhu J, Li Z, Guo J. Mathematical and experimental analysis on solar thermal energy harvesting performance of the textile-based solar thermal energy collector. Renewable Energy 2018;129:553–60. https://doi.org/10.1016/j.renene.2018.05.097.
[5] Zabek D, Morini F. Solid state generators and energy harvesters for waste heat recovery and thermal energy harvesting. Therm Sci Eng Prog 2019;9:235–47. https://doi.org/10.1016/j.tsep.2018.11.011.
[6] Sun W, Zhao D, Tan T, Yan Z, Guo P, Luo X. Low velocity water flow energy harvesting using vortex induced vibration and galloping. Appl Energy 2019;251:113392. https://doi.org/10.1016/j.apenergy.2019.113392.
[7] Dai HL, Abdelkefi A, Wang L. Piezoelectric energy harvesting from concurrent vortex-induced vibrations and base excitations. Nonlinear Dyn 2014;77(3):967–81. https://doi.org/10.1007/s11071-014-1355-8.
[8] Silva-Leon J, Cioncolini A, Nabawy MR, Revell A, Kennaugh A. Simultaneous wind and solar energy harvesting with inverted flags. Appl Energy 2019;239:846–58. https://doi.org/10.1016/j.apenergy.2019.01.246.
[9] Zhang L, Abdelkefi A, Dai H, Naseer R, Wang L. Design and experimental analysis of broadband energy harvesting from vortex-induced vibrations. J Sound Vib 2017;408:210–9. https://doi.org/10.1016/j.jsv.2017.07.029.
[10] Bao C, Dai Y, Wang P, Tang G. A piezoelectric energy harvesting scheme based on stall flutter of airfoil section. Eur J Mech B Fluids 2019;75:119–32. https://doi.org/10.1016/j.euromechflu.2018.11.019.
[11] Javed U, Abdelkefi A. Role of the galloping force and moment of inertia of inclined square cylinders on the performance of hybrid galloping energy harvesters. Appl Energy 2018;231:259–76. https://doi.org/10.1016/j.apenergy.2018.09.141.
[12] Parkinson GV, Smith JD. The square prism as an aeroelastic non-linear oscillator. Quart J Mech Appl Math 1964;17(2):225–39.
[13] Ewere F, Wang G, Cain B. Experimental investigation of galloping piezoelectric energy harvesters with square bluff bodies. Smart Mater Struct 2014;23(10):104012. https://doi.org/10.1088/0964-1726/23/10/104012.
[14] Dai H, Yang Y, Abdelkefi A, Wang L. Nonlinear analysis and characteristics of inductive galloping energy harvesters. Commun Nonlinear Sci Numer Simul 2018;59:580–91. https://doi.org/10.1016/j.cnsns.2017.12.009.
[15] Hémon P, Amandolese X, Andrianne T. Energy harvesting from galloping of prisms: a wind tunnel experiment. J Fluids Struct 2017;70(Supplement C):390–402.
[16] Wang J, Tang L, Zhao L, Zhang Z. Efficiency investigation on energy harvesting from airflows in HVAC system based on galloping of isosceles triangle sectioned bluff bodies. Energy 2019;172:1066–78. https://doi.org/10.1016/j.energy.2019.02.002.
[17] Sirohi J, Mahadik R. Harvesting wind energy using a galloping piezoelectric beam. J Vib Acoust 2011;134(1). https://doi.org/10.1115/1.4004674.
[18] Yang Y, Zhao L, Tang L. Comparative study of tip cross-sections for efficient galloping energy harvesting. Appl Phys Lett 2013;102(6):064105.
[19] Hu G, Tse K, Wei M, Naseer R, Abdelkefi A, Kwok K. Experimental investigation on the efficiency of circular cylinder-based wind energy harvester with different rod-shaped attachments. Appl Energy 2018;226:682–9. https://doi.org/10.1016/j.apenergy.2018.06.056.
[20] Liu F-R, Zhang W-M, Peng Z-K, Meng G. Fork-shaped bluff body for enhancing the performance of galloping-based wind energy harvester. Energy 2019;183:92–105. https://doi.org/10.1016/j.energy.2019.06.044.
[21] Zhou C-F, Zou H-X, Wei K-X, Liu J-G. Enhanced performance of piezoelectric wind energy harvester by a curved plate. Smart Mater Struct 2019;28(12):125022. https://doi.org/10.1088/1361-665x/ab525a.
[22] Tucker Harvey S, Khovanov IA, Denissenko P. A galloping energy harvester with flow attachment. Appl Phys Lett 2019;114(10):104103. https://doi.org/10.1063/1.5083103.
[23] Abdelkefi A, Hajj MR, Nayfeh AH. Piezoelectric energy harvesting from transverse galloping of bluff bodies. Smart Mater Struct 2012;22(1):015014. https://doi.org/10.1088/0964-1726/22/1/015014.
[24] Ragheb M, Ragheb AM. Wind turbines theory – the Betz equation and optimal rotor tip speed ratio. In: Carriveau R, editor. Fundamental and advanced topics in wind power. Rijeka: IntechOpen; 2011. p. 2. Ch. 2.
[25] Ellington CP, van den Berg C, Willmott AP, Thomas ALR. Leading-edge vortices in insect flight. Nature 1996;384(6610):626–30. https://doi.org/10.1038/384626a0.
[26] Muijres FT, Johansson LC, Barfield R, Wolf M, Spedding GR, Hedenström A. Leading-edge vortex improves lift in slow-flying bats. Science 2008;319(5867):1250–3. https://doi.org/10.1126/science.1153019.